RSC Advances

PAPER

View Article Online
View Journal | View Issue

Cite this: *RSC Adv.*, 2025, **15**, 45283

Corrosion mechanism of Cr-rich nickel-based alloys in a ternary molten salt: morphology analysis and first-principles study of Cl adsorption

Wenhao Zhao,[a] Dongkai Ni,[b] Wenjie Qi,[a] Jing Ding,[b] Jianfeng Lu,[b] Weilong Wang,[b] Xiaolan Wei*[a] and Shule Liu *[b]

The corrosion of metal materials by chloride molten salts has limited their high-temperature application as heat transfer/storage media, while the composition of alloys strongly affects the corrosiveness of molten salts. This work combines experiments and first-principles calculations to study the long-term corrosion mechanism at the interface between nickel-based alloys and NaCl–$CaCl_2$–$MgCl_2$ chloride molten salts. The findings indicate the considerable depletion of chromium within the metallic stratum situated beneath the corrosion oxide layer of chromium-enriched alloys. The corrosion morphology shows that the Cr-rich alloys Hastelloy C-276 and Hastelloy X produce many holes in their cross-section, with $MgCr_2O_4$ formed on their surface, while Hastelloy B-2 has fewer stable oxidation products on its surface and no $MgCr_2O_4$ is generated. First-principles calculations focusing on Cl atom adsorption suggest that the reaction process of Cl atoms on the surface of doped Cr (Fe or Mo)–Ni (111) crystals is the key to Cr loss, and the results show that the doped Cr–Ni (111) crystal surface exhibited a larger adsorption energy for Cl, higher charge transfer amount, and lower desorption energy for the corrosion product $CrCl_4$. The segregation energy difference of transferring a doped Cr atom from the second layer to the top surface layer is only 0.04 eV, while the adsorbed Cl is located around Cr on the Cr–Ni (111) crystal surface, indicating continuous Cr loss during the corrosion process. Therefore, if Cl atoms in molten salts are prevented from forming an adsorption layer on the alloy surface, the corrosion of Cr-rich nickel alloys in chloride molten salts can be reduced.

Received 9th July 2025
Accepted 10th October 2025

DOI: 10.1039/d5ra04910e

rsc.li/rsc-advances

1. Introduction

Concentrating solar power (CSP) plants can provide low-cost power and are potential power plants for sustainable development in the future. The optimal operational temperature for the forthcoming generation of concentrating solar power (CSP) technology is in excess of 700 °C. Molten salts are frequently utilized as heat transfer fluid in CSP systems. In comparison to commercial nitrates, chloride molten salts exhibit analogous thermophysical properties, superior operating temperature, enhanced thermal stability, and reduced cost, thereby making them a prospective medium for heat storage and promising fluid for the next generation of concentrated solar power (CSP) systems.[1] However, the strong corrosion of metals by chloride molten salts at high temperatures limits their application.

Metal structural materials such as nickel- and iron-based alloys contain other metallic elements (Mo, Cr, W, *etc.*) to enhance their corrosion resistance, strength and other properties,[2] which characterize the structural stability of these materials under corrosion. However, controversy remains regarding the impact of these elements on the corrosion of alloys in high temperature molten salts, particularly in regard to the role of chromium. In a study conducted by Wang *et al.*,[3] the corrosion of pure Fe and pure Cr in $ZnCl_2$ molten salt was examined. The findings indicated that metal Cr exhibited a comparatively reduced corrosion degree in comparison to Fe. Vignarooban *et al.*[4] investigated the corrosion behavior of three nickel-based alloys, Hastelloy N, C276 and C22, in NaCl–KCl–$ZnCl_2$ ternary chloride molten salt. The findings indicated that the Cr element could serve as a protective measure for the alloy. However, Hastelloy N, which exhibited the lowest Cr content, demonstrated a significant degree of corrosion. Thus, it can be surmised that the Cr element in the alloy serves to provide protection in the NaCl–KCl–$ZnCl_2$ molten salt.

Liu *et al.*[5] conducted a comparative analysis of the corrosion behavior of an Ni–Mo–Cr alloy exposed to two distinct environments, liquid salt and vaporized chloride molten salt. Their findings revealed that the alloy exhibited significant Cr depletion on the corrosion surface within the molten salt, with the depth of Cr depletion in molten salt steam being nearly twice

[a]*School of Chemistry and Chemical Engineering, South China University of Technology, Guangzhou 510640, PR China. E-mail: xlwei@scut.edu.cn*
[b]*School of Materials Science and Engineering, Sun Yat-sen University, Guangzhou High Education Mega Center, Guangzhou 510006, PR China. E-mail: liushle@mail.sysu.edu.cn*

that observed in liquid salt. In the study of the corrosion behavior of ferritic-martensitic P91 and stainless steel SS304 in NaCl–KCl–$MgCl_2$ molten salt, Gong *et al.*[6] observed the emergence of numerous missing cracks in the cross-sectional analysis of SS304 specimens that had been subjected to corrosion in molten salt for 1400 h. However, this phenomenon was not observed in the case of P91. Liu *et al.*[7] found that the corrosion layer of Cr-rich alloy exhibits obvious Cr deficiency phenomenon, while the alloy with less Cr does not, and it is speculated that more Cr in alloys has an adverse effect on the loss of chromium during corrosion. Although the above-mentioned studies and others have found that some Cr-containing metals exhibit Cr loss in different chloride molten salts, there are still insufficiencies in the research on the loss of alloy elements of candidate structural materials in chloride molten salts, and the results of various metal elements seem to be contradictory.[8,9]

Existing studies have focused on corrosion experiments of alloys in molten salts, while the drivers of elemental loss and atomic-scale mechanisms are still poorly understood. First-principles calculation based on quantum mechanics is a powerful tool for studying microscopic corrosion mechanisms and has been applied in recent years in the study of corrosion mechanisms in fluoride molten salts. Yu *et al.*[10] investigated the segregation behavior of some transition metals on the surface of Ni (111) and concluded that the elemental segregation behavior is closely related to the surface energy difference and elastic potential energy between the elemental alloy bodies. Yin *et al.*[11] simulated the effect of F atom adsorption on the segregation of Cr on the surface of nickel in a fluoride salt environment by first principle calculations, and found that the adsorption of F atoms would significantly lead to the segregation of Cr on its surface. Nam *et al.* used the first-principles molecular dynamics (FPMD) method to calculate the diffusion rate and local structure of Cr^0, Cr^{2+} and Cr^{3+} in LiF–BeF_2 and LiF–NaF–KF molten salts, and found that with an increase in the valence state charge, the coordination number of Cr in the molten salts increased and the diffusion rate slowed down.[12] Austin *et al.*[13] studied the 0–6 valence coordination structure of Mo in LiF–NaF–KF molten salt. The higher valence Mo will form dimers or trimers in the molten salt, and the 4 valence Mo is the highest valence state that can exist stably in the molten salt. The higher valence Mo is easy to overflow the system in a gaseous state. Chahal used FPMD to study the effect of ZrF_4 mole fraction and temperature on the coordination structure of the LiF–NaF–ZrF_4 system.[14] It was found that the average coordination number decreased with an increase in composition and temperature, which was consistent with the results of Raman spectroscopy. In addition, many researchers have determined the thermophysical properties and microstructure of F–LiNaK molten salt by calculation.[15–19] Startt *et al.*[20] simulated and calculated the effect of possible anion–cation interactions in chloride and fluoride salts on Cr segregation on the Ni (100) surface.

In general, the existing research lacks the interpretation of the nature of Cr loss from the perspective of adsorption and reaction and the difference in the segregation of elements in the alloy in molten salt corrosion. The influence of trace elements in alloys on the corrosion mechanisms in molten salts is still poorly understood, especially with regard to the effect of chloride salts.[21] The impact of chloride adsorption on the segregation and dissolution of Cr, Fe, and Mo on the alloy surface is still not fully elucidated.

Herein, to gain better insight into the corrosion of Cr-rich nickel-based alloys in chloride-ion molten salts, the long-term corrosion behavior of two Cr-rich alloys and one Cr-poor nickel-based alloy in NaCl–$MgCl_2$–$CaCl_2$ salts is investigated. The reaction process of Cl atoms adsorbed on the surface of doped Cr (Fe or Mo)–Ni (111) crystals was also systematically determined using first-principles calculations. The microscopic mechanism of the loss is further revealed. This work provides insight into the development of methods to inhibit the corrosion of nickel-based alloys in chloride molten salts.

2. Experimental

2.1 Materials

The ternary NaCl–$MgCl_2$–$CaCl_2$ eutectic molten salt (39.5 : 39.1 : 21.4 wt%) was prepared by using commercially available NaCl (purity ≥99.5 wt%), $MgCl_2$ (purity ≥99 wt%) and $CaCl_2$ (purity ≥96 wt%).[7] The three salts were initially subjected to drying at 120 °C, after which they were combined in an alumina crucible in accordance with the prescribed ratio. The crucible was positioned within a muffle furnace, maintained at a temperature of 250 °C, and subsequently subjected to a 3 h drying procedure. Afterwards, drying was continued at 600 °C for 2 h. Once the mixture cooled to room temperature, the desired NaCl–$MgCl_2$–$CaCl_2$ ternary chloride salt (TCS) was obtained by crushing the material. The main thermophysical properties of TCS are listed in Table 1.[22]

Three types of alloys, Hastelloy X (HX), Hastelloy C-276 (HC-276) and Hastelloy B-2 (HB-2), were used for the corrosion experiments in this study. The main compositions of these alloys are shown in Table 2. Each alloy sample was mechanically divided into a 40 mm × 15 mm × 1 mm piece and the sample surface was polished with 10 μm SiC sandpaper before the experiment. Subsequently, the surface of each sample was polished to a mirror finish using a 2.5 μm diamond-based polish.

Table 1 Main physical properties of TCS

Sample	Melting point/°C	Fusion enthalpy/J g^{-1}	Specific heat capacity (c_p)/J g^{-1} K^{-1}	Density (ρ)/g cm^{-3}	Thermal conductivity (λ)/W m^{-1} K^{-1}
TCS	427.5	190.1	1.112 (600 °C)	2.349 (550 °C)	0.404 (480 °C)

Table 2 Main composition of the samples (wt%)

Alloy	Ni	Cr	Fe	Mo	Other
Hastelloy X	42–52	20.5–23.0	17.0–20.0	8.0–10.0	Co ≤ 1.0
Hastelloy C-276 (HC-276)	51–59	14.5–16.5	4.0–7.0	15.0–17.0	W 3.0–4.5 Co ≤ 2.5, Mn ≤ 1.0, V 0 ≤ 0.35
Hastelloy B-2	65–70	0.4–0.7	1.6–2.0	26.0–30.0	Co ≤ 3.0

Following a washing process involving deionized water and anhydrous ethanol, the samples were dried in an oven for future use.

2.2 Corrosion and analysis method

The treated alloy was placed in a crucible, with 300 g of TCS added to completely submerge the alloy, and then the crucible was covered with a lid. The crucible was placed in a muffle furnace, ramping the temperature to 600 °C (temperature above the TCS eutectic at which the salt remains stable) at 5 °C min^{-1}, and held for 35 days. Following the completion of the aforementioned corrosion experiments, the alloy samples were treated in accordance with the methodology outlined in the ASTM G1-03 standards.[23]

Physical analyses of the specimens before and after corrosion were carried out using a multi-position auto-sampling X-ray diffractometer (XRD; X'pert Powder, Panacor, The Netherlands). The morphology of the specimen cross-section was analyzed by scanning electron microscopy, prior to and following the corrosion process (SEM; Hitachi Model 3700N, Japan), and the cross-section morphology was analyzed by using polymer embedding, where the sample to be characterized was encased in resin and polished to expose its cross-section. Concurrently, an energy dispersive spectrometer (EDS) was employed to ascertain the distribution of elements within the specimen cross-section, thereby discerning the diminution of alloying elements within the specimen cross-section.

2.3 Computational method and details

To explore the microscopic mechanism of the loss of alloying elements during the corrosion process of Cr-rich nickel-based alloy materials in NaCl–$MgCl_2$–$CaCl_2$ salt, the first-principles method based on density functional theory (DFT) was used to systematically calculate the reaction process of Cl atoms adsorbed on the surface of doped Cr (Fe or Mo)–Ni (111) crystals. The Cl atoms are in the form of Cl^- ions, which are formed through the process of oxidation by dissolved O_2 in the molten salt.

The bulk structure of Ni crystals was first constructed to carve out the Ni surface model. Based on the face-centered cubic (fcc) single cell of Ni crystal, the *k*-points are set to 25 × 25 × 25. The calculated lattice constant of the Ni crystal is 3.518 Å. The surface energy and surface work function of three low-index crystal planes in the Ni cell were calculated, and the low-index crystal plane with a stable crystal was selected as the research target. Then, an Ni-based alloy crystal surface containing Cr, Fe or Mo was created by replacing a single Ni atom with Cr, Fe or Mo, respectively. Among them, the Ni atoms in the bottom two layers of the model are fixed, and in the four layers from the surface to the inside, one Ni atom in each layer is replaced and numbered by Cr, Fe or Mo atoms, respectively (see Fig. 1).

All first-principles calculations were performed using density functional theory (DFT) and Born–Oppenheimer approximation, which are implemented in the Vienna *Ab Initio* Simulation Package (VASP).[24–26] The exchange–correlation functional was treated with the generalized gradient approximation (GGA) and the Perdew–Burke–Ernzerhof (PBE) exchange–correlation functional,[27] and the electron–ion interactions were approximated by pseudopotentials developed using the projector augmented wave (PAW) method.[28,29] The valence electrons considered in the calculation are as follows: Cl ($3s^2 3p^5$), Ni ($3d^8 4s^2$), Fe ($3d^6 4s^2$), Cr ($3d^5 4s^1$), and Mo_sv ($4p^6 4d^5 5s^1$). The energy cutoff value for the plane wave was set to 450 eV, and the energy convergence threshold of the self-consistent iteration is 10^{-6} eV. The convergence criterion for geometric optimization is that the force acting on each atom is reduced to below 0.01 eV $Å^{-1}$, which is the limit of the optimization. In all structural relaxation calculations, the first-order Methfessel–Paxton smear method was used with a smear width of 0.2 eV. The gamma

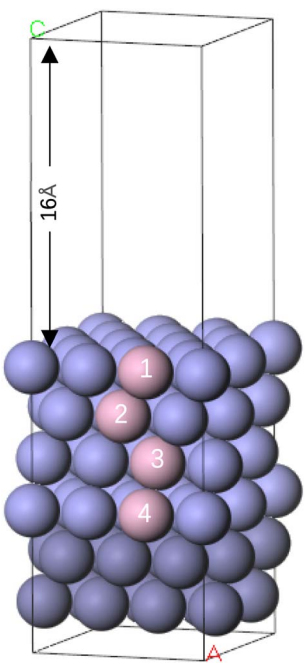

Fig. 1 Surface model used for simulating the doping and segregation of Cr, Fe or Mo elements. The numbered pink spheres are doped with Cr, Fe or Mo atoms to simulate the different layers of Cr, Fe or Mo on the Ni (111) surface, and the unnumbered blue spheres are Ni atoms.

method was used to construct the inverted space K points, and a 5 × 5 × 1 grid was used to divide the Brillouin zone. Furthermore, all calculations were conducted using spin-polarized density functional theory to accurately depict the behavior of unpaired electrons in the valence shell.

3. Results and discussion

3.1 Morphology of the cross-section and element distribution

Fig. 2 illustrates the morphology of the cross-section and element distribution of the HX, HC-276 and HB-2 alloy samples corroded in the TCS at 600 °C for 35 days.

Fig. 2 shows that the region of O distribution on the alloys surface is relatively thin, especially on HC276 and HB-2. This might be due to the short corrosion time or the insufficiency supply of oxygen, which may come from the water vapor or the air[7] during the corrosion process. The Mo distributions in the corrosion layer and metal matrix are not much different from each other. The Mg element is distributed in the same area with O and Cr in the alloys, which suggests that some compounds are formed with them.

The elemental distributions shown in Fig. 2 indicate that there are Cr and Fe loss zones between the oxide layer and the metal matrix of the Cr-rich alloys HX and HC-276. In the Cr loss area of HX and HC-276, the content of Ni is more than that of the metal matrix, which may be due to the increase in Ni relative content in this area resulting from the loss of Cr and Fe. This

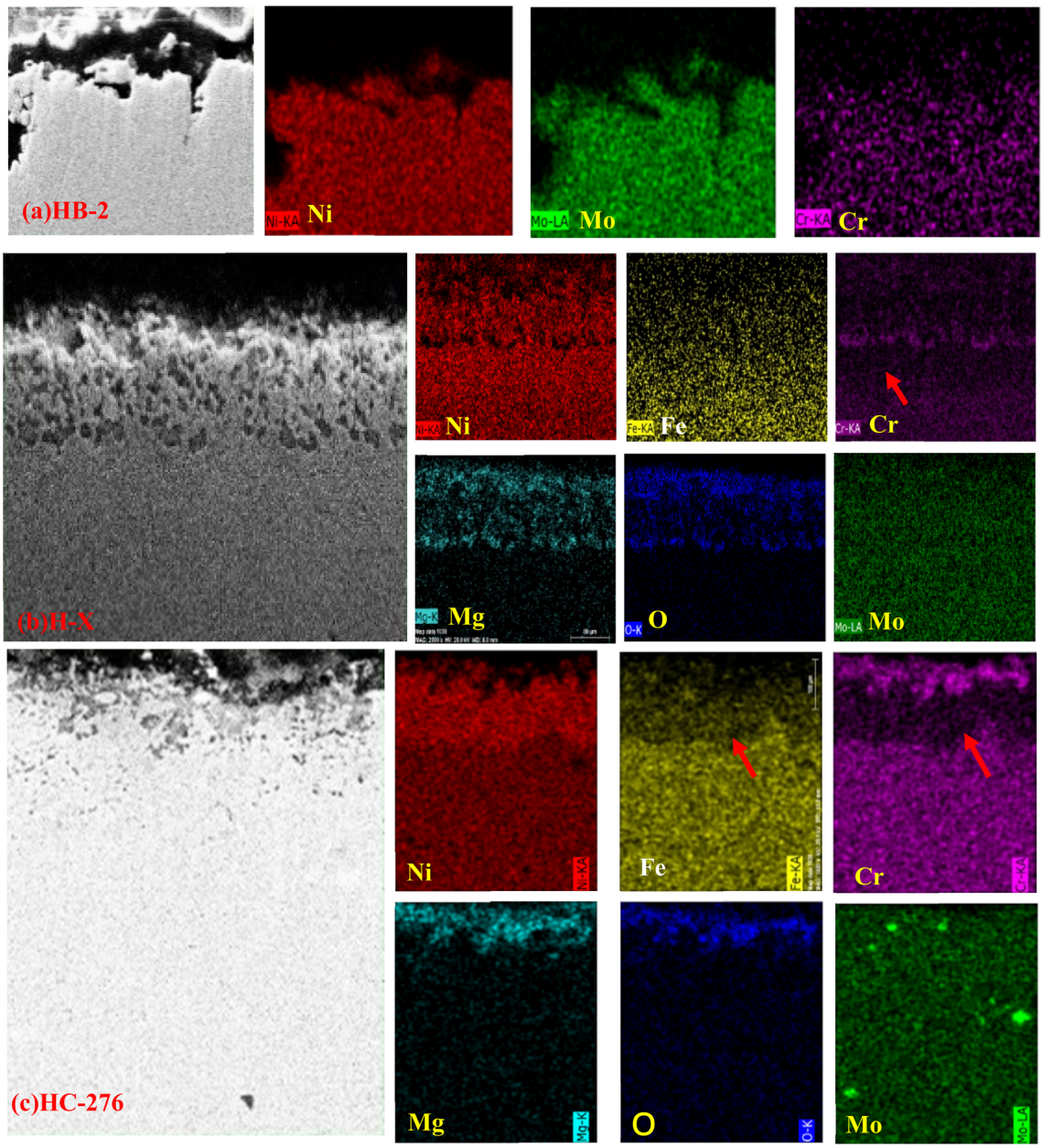

Fig. 2 SEM images of cross-section and the elemental distributions of (a) HB-2, (b) H-X and (c) HC-276.

phenomenon of Cr loss is consistent with the observations in other Cr-rich nickel-based alloys.[5–7]

3.2 Phase structure analysis of corrosion products

The X-ray diffraction patterns of the corrosion products covered on the surfaces of the HC-276, HB-2 and HX alloy samples after the corrosion experiment are presented in Fig. 3(a)–(c), respectively.

Fig. 3 shows that the three alloys retain their phase structure to a large extent after 35 days of corrosion. There is no obvious diffraction peak of oxide product in HB-2. The diffraction peaks of the corrosion product from HC-276 are relatively small. The peaks of corrosion product in HX are mainly attributed to $MgCr_2O_4$, combining the cross-sectional line scan and element distribution map images of EDS (Fig. S1 of the SI). The corrosion product $MgCr_2O_4$ was also observed on the surface of Inconel625 alloy corroded in TCS.[7]

Based on the EDS and XRD analysis, it is speculated that the reactions related to Cr loss occur during the corrosion process of Cr-rich alloys in TCS, as shown in Fig. 4.

The Gibbs free energy changes of the reactions in Fig. 4 are all negative,[7] indicating that the chlorides can be oxidized by the O_2 molecules dissolved in the molten salt, forming Cl_2. The formed Cl_2 may diffuse into the interior of the metal along the corrosion crack, causing the continuous loss of Cr during corrosion.

Cl atoms may also be generated and adsorbed onto the metal surface at the microscopic level, promoting the subsequent chlorination corrosion reaction. To further explore the role of Cl atoms in corrosion reactions, we established an M-doped nickel crystal structure, where M standards for the doped metal elements. After that, the first-principles structural optimization method was used to calculate the chlorination reaction process and its energy changes and reveal the mechanism of Cr loss in Cr-rich alloys during the corrosion process.

3.3 Microanalysis of corrosion mechanism

3.3.1 Cl adsorption on surfaces. In the process of metal polycrystalline formation, the most stable low index crystal plane grows preferentially, and thus the probability of exposure

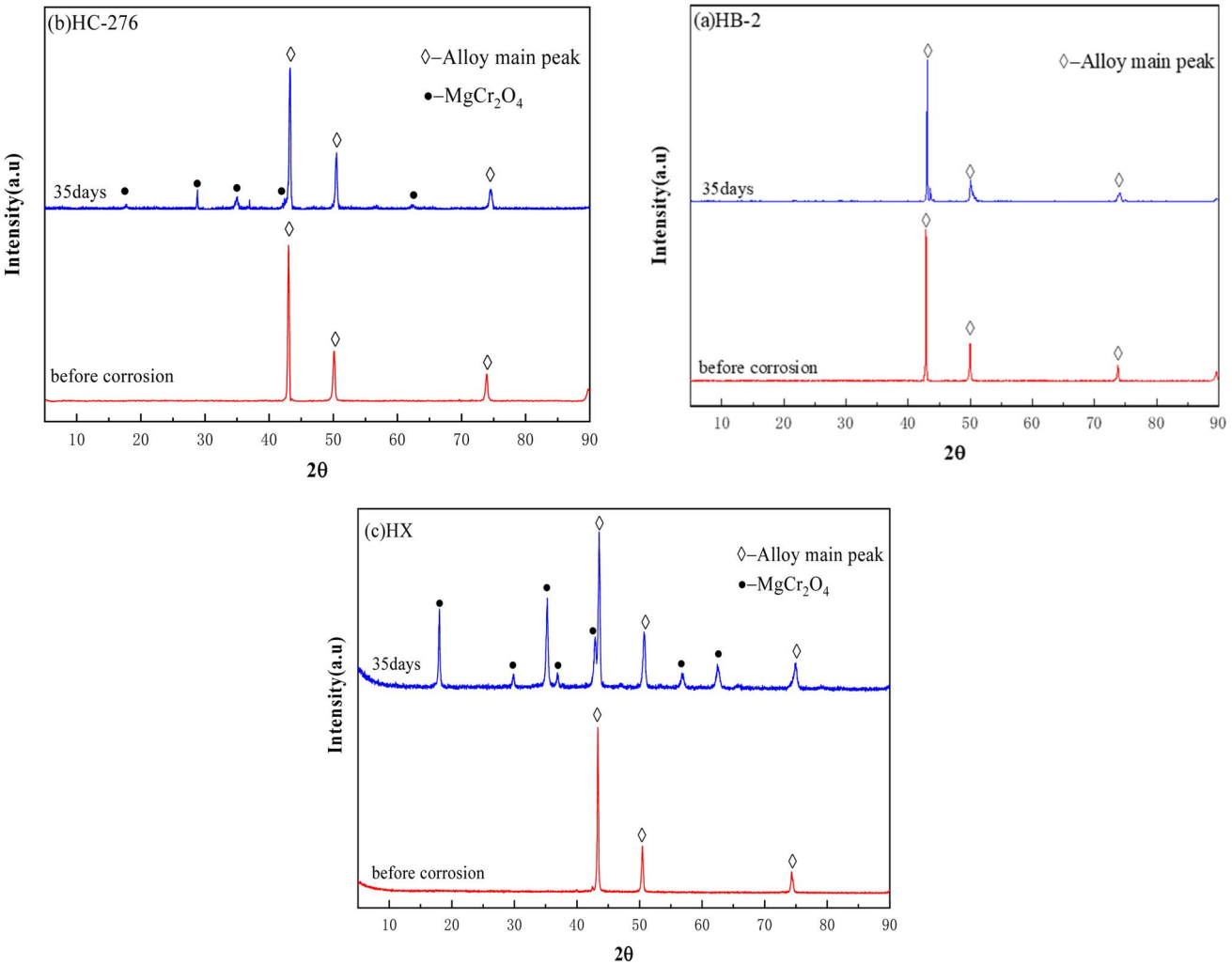

Fig. 3 XRD patterns of (a) HB-2, (b) HC-276 and (c) HX pre-corrosion and post-treatment after corrosion for 35 days in NaCl–$MgCl_2$–$CaCl_2$ molten salt at 600 °C.

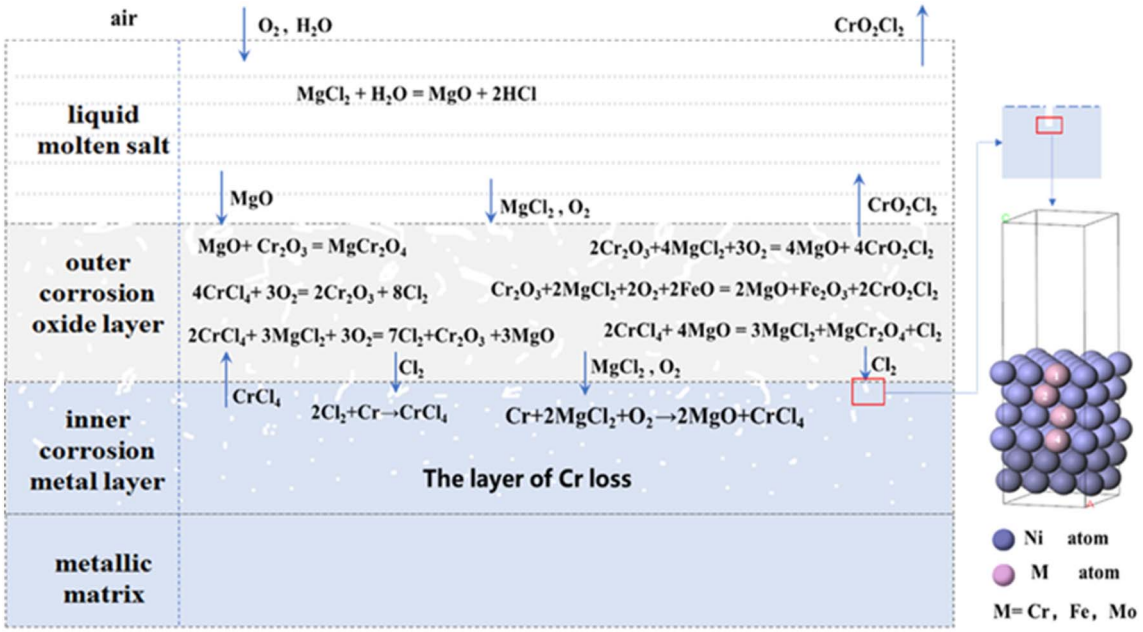

Fig. 4 Possible reactions of Cr-rich metals in TCS.

of the metal surface is larger, and the probability of its corrosion in molten salt is also larger.

As listed in Table 3, the results calculated in this work are close to the literature values. The Ni (111) crystal plane has the highest work function and the lowest surface energy, and is the most stable low-index crystal plane, suggesting that the Ni (111) plane has the highest exposure probability and preferential corrosion in molten salt. Therefore, the Ni (111) surface is identified as the primary surface for molten salt ion adsorption in this study.

The adsorption energy of one Cl atom at various sites on the Ni (111) surface and the M–Ni (111) surface was calculated as follows:

$$E_{\text{adsorption}} = E_{\text{slab-adsorbate}} - (E_{\text{slab}} + E_{\text{adsorbate}}) \quad (1)$$

where $E_{\text{slab-adsorbate}}$ is the total energy of the adsorbed atom on the surface of Ni (111) surface and M–Ni (111), E_{slab} is the total energy of the adsorbate-free relaxed surface, and $E_{\text{adsorbate}}$ is the energy of Cl atom.

The adsorption energy difference of one Cl atom at various sites on the Ni (111) surface and the M–Ni (111) surface was calculated to ascertain the most stable adsorption site for the Cl atom on the crystal plane. This was then used to determine the initial site of corrosion. Fig. 5 illustrates the adsorption sites of the Ni (111) surface and the M–Ni (111) surface. The adsorption energies of Cl atoms at different sites on Ni (111) or M–Ni (111) surfaces were calculated and presented in Table 5.

Before calculating the adsorption energy, we verified the stability of the M–Ni system by calculating the formation energy, as follows:

$$E_{\text{form}} = E_{\text{M-Ni}} - E_{\text{Ni}} - \mu_{\text{Cr}} + \mu_{\text{Ni}} \quad (2)$$

where E_{form} denotes the formation energy of the doped system, $E_{\text{M-Ni}}$ represents the total energy of the host system with the dopant incorporated, E_{Ni} signifies the total energy of the pristine (undoped) host system, and μ is the chemical potential of the dopant element in its reference state. The calculated formation energies for the M–Ni systems are provided in Table 4.

The formation energies of all the doped systems are negative, indicating that the doping of Fe, Cr, and Mo in the Ni matrix is thermodynamically feasible.

During the structure optimization calculation, it was found that when Cl is adsorbed on the bridge site of the Ni (111) surface, it is easy to slip to the FCC site; when Cl is adsorbed on the TOP2 and bridge sites of the M–Ni (111) surface, it is also easy to slip to the FCC1 site, indicating that the TOP2 and bridge sites cannot adsorb Cl.

According to the values of the adsorption energy shown in Table 5, one Cl atom is preferentially adsorbed at the FCC1 site closest to Mo, Cr or Fe in M–Ni (111), and the FCC site in Ni (111). The adsorption energy of Cl at the FCC1 site of the M–Ni (111) surface is −2.328 eV (Cr), −2.121 eV (Fe) and −2.338 eV (Mo), respectively, which is larger than that of −2.064 eV at the

Table 3 Calculated values of surface energy and work function of low-index crystal plane of nickel

	Surface energy/(J m^{-2})		Work function/eV	
Crystal face	Calculation	Reference[30,31]	Calculation	Reference[30,31]
Ni (111)	1.92	1.94, 1.92	5.06	5.00, 5.10, 5.35
Ni (100)	2.20	2.21, 2.21	4.94	4.90, 4.95, 5.22
Ni (110)	2.29	2.34, 2.29	4.46	4.46, 4.43, 5.04

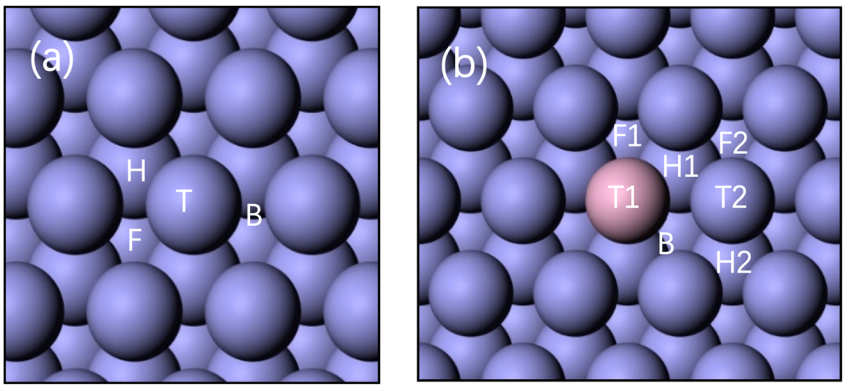

Fig. 5 Surface adsorption sites on (a) Ni (111) and (b) M–Ni (111) surfaces, where the atoms at the T1 site are doped Cr, Fe or Mo. T, F, H and B symbols represent the TOP, FCC, HCP, and bridge sites, respectively.

Table 4 Formation energy of M–Ni

	Cr–Ni	Fe–Ni	Mo–Ni
E_{form} (eV)	−0.09	−0.31	−0.10

FCC site on the Ni (111) surface. This means that doping Mo, Cr or Fe in the Ni (111) plane may promote Cl adsorption and probability of the chlorination reaction.

According to the adsorption energy of Cl, Mo has the strongest adsorption capacity for one Cl. However, experiments show that Cr is most likely to be lost after corrosion. Considering that the adsorption of Cl is the early stage of corrosion, the adsorption of multiple Cl, the transfer of charge after Cl adsorption, the desorption of products, and the migration of doped atoms in Ni crystal should also be considered.

3.3.2 The effect of adsorbed Cl atoms on the charge transfer of doped Ni (111) crystal. After the adsorption of Cl on the Ni (111) or doped M–Ni (111) surface, the charge transfer to Cl from the metal atoms is the core part of the corrosion reaction. Table 6 shows the Bader charge of each atom around the doped atom after adsorbing a Cl atom on the most stable FCC or FCC1 site of the Ni (111) or M–Ni (111) surface. The Bader charge value can explain the charge transfer of the atoms near the stable adsorption site. Among them, the Ni atom is the adjacent atom of the FCC site with adsorbed Cl. Due to symmetry, the charge transfer amounts of three Ni atoms adjacent to Cl at the FCC site of Ni (111) are very close.

As shown in Table 6, doping the Cr (Fe or Mo) atom promotes the charge transfer from the metal atoms to Cl because the charge gain of Cl in Cr (Fe or Mo)–Ni (111) is larger than that in Ni (111). On the Cr–Ni (111) surface, the Ni adjacent to the adsorbed Cl at the FCC1 site loss $+0.065e_0$ charge, which is much less than that of $+0.126e_0$ charge. This means that when the Cl is adsorbed at the site of FCC1, the doped Cr will play a protective role for Ni, and the same role for Fe or Mo.

Table 6 shows the MCl-type adsorption and that its preferential adsorption site of Cl on the M–Ni (111) surface is FCC1 site. In the case of MCl_2-type adsorption, further structural optimization found that if one Cl is placed at the FCC1 position, the other Cl will be located at the HCP1 position opposite to the FCC1 position because the energy of this type of adsorption is the lowest. The MCl_3-type adsorption is the case that three Cl atoms are dispersed at three FCC1 sites and maintain symmetry, where the Cl atoms will slightly deviate from the FCC1 site, which is caused by the repulsive coulombic force and the van der Waals forces between Cl atoms. In the case of MCl_4-

Table 6 Charge transfer amount (e_0) of each atom after Cl is adsorbed at the most stable adsorption site on Ni (111) and doped M–Ni (111) surfaces[a]

	Ni (111)	Cr–Ni (111)	Fe–Ni (111)	Mo–Ni (111)
Ni	+0.126	+0.065	+0.086	+0.067
M	—	+0.743	+0.488	+0.757
Cl	−0.457	−0.491	−0.486	−0.474
tot	−0.079	+0.382	+0.174	+0.417

[a] In table, M refers to the doped atoms Cr, Fe, Mo; the positive value means charge loss, and the negative means charge gain; 'tot' is the algebraic sum of the charge transfer amounts of the three Ni atoms adjacent to the adsorbed Cl at FCC, or that of two Ni atoms and a Cr (Fe or Mo) atom adjacent to the adsorbed Cl at FCC1 site.

Table 5 Adsorption energy of Cl at different sites on Ni (111) and M–Ni (111) surfaces

Adsorption site	TOP	HCP	FCC	TOP1	HCP1	HCP2	FCC1	FCC2
Ni (111)	−1.517	−2.013	−2.064					
Cr–Ni (111)				−1.964	−2.238	−2.000	−2.328	−2.033
Fe–Ni (111)				−1.675	−2.063	−2.017	−2.121	−2.059
Mo–Ni (111)				−2.273	−2.250	−1.957	−2.338	−1.968

Table 7 Charge transfer amounts (e_0) of atoms near doped Ni (111) surface after adsorbing multiple Cl

	MCl_2			MCl_3		MCl_4		
Doped atom	M	Cl(HCCP)	Cl(FCC)	M	Cl(FC)C	M	Cl(FCC)	Cl (TOP)
Cr	+0.831	−0.483	−0.481	+0.916	−0.481	+0.984	−0.481	−0.484
Fe	+0.550	−0.473	−0.474	+0.637	−0.466	—	—	—
Mo	+0.976	−0.470	−0.464	+0.953	−0.462	+0.946	−0.460	−0.465

type adsorption, three Cl atoms are placed at the FCC1 sites, and the fourth Cl atom is placed at TOP site of the M atom. After structural optimization, the Cl atoms will move slightly from the original adsorption site because of atom repulsion. The optimized configurations of MCl_2, MCl_3 and MCl_4 on the M–Ni (111) surface are shown in Fig. S2 of the SI and the corresponding charge transfer amounts obtained are listed in Table 7, where the positive or negative values mean charge loss or gain, respectively.

Table 7 shows that Cr is easier to transfer charge to Cl, regardless of MCl_2-type, MCl_3-type or MCl_4-type adsorption. In $CrCl_4$-type adsorption, Cr lost the most charge of $+0.984e_0$ and four Cl obtained the most total charge of $-1.927e_0$ ($-0.481 \times 3 + 0.484$) compared to the other types of adsorption. The difference in Cr loss charge and total gain charge of four Cl is $-0.943e_0$ (+0.984–1.927), indicating that four Cl atoms around Cr need to obtain more charge from the surrounding Ni atoms, and then promote corrosion.

In the case of MCl_3-type adsorption, the magnitude of the three types of Cl total charge gain is $-1.443e_0$ (Cr) > $-1.398e_0$ (Fe) > $-1.386e_0$ (Mo), which is greater than the charge loss of Cr ($+0.916e_0$), Fe ($+0.637e_0$) and Mo ($+0.953e_0$), respectively. In the case of MCl_2-type adsorption, the total charge gain of two types of Cl from doped atoms is $-0.964e_0$ (Cr) > $-0.947e_0$ (Fe) > $-0.934e_0$ (Mo), which is also greater than the charge loss of Cr ($+0.831e_0$) and Fe ($+0.550e_0$). In $MoCl_2$-type adsorption, the total charge gain of two Cl is $-0.934e_0$, which is smaller than the charge loss of Mo ($+0.976e_0$), indicating that that the excess charge lost by Mo has been transferred to the surrounding Ni to protect Ni.

By evaluating the differential charge density, the charge transfer near the doped atom can be visually displayed while a Cl atom is adsorbed. The calculation of the differential charge density is based on the following equation:

$$\Delta\rho = \rho_{tot} - \rho_{slab} - \rho_{Cl} \quad (3)$$

where ρ_{tot} is the total charge density of the whole system after adsorbing Cl, ρ_{slab} is the charge density of the surface before adsorption, and ρ_{Cl} is the charge density of the Cl atom. Fig. 6 shows the difference charge density diagram of the Cr (Fe or Mo)–Ni (111) surfaces with MCl_3-type adsorption. Fig. 6(a)–(c) show their three-dimensional map with the isosurface density of $\pm$ 0.003 e $Å^{-1}$, respectively. The blue area indicates electron cloud dissipation, while the yellow area indicates electron cloud aggregation.

Fig. 6(a)–(c) show that three Cl atoms are chemically adsorbed on the M–Ni (111) surfaces around the doped M atom. The electron cloud around Cl around Cr (Fe or Mo) accumulates significantly, while the electron cloud around of Cr (Fe or Mo) dissipates, and the electron cloud aggregation area is pointing to the doped Cr (Fe or Mo) atom, rather than Ni atoms,

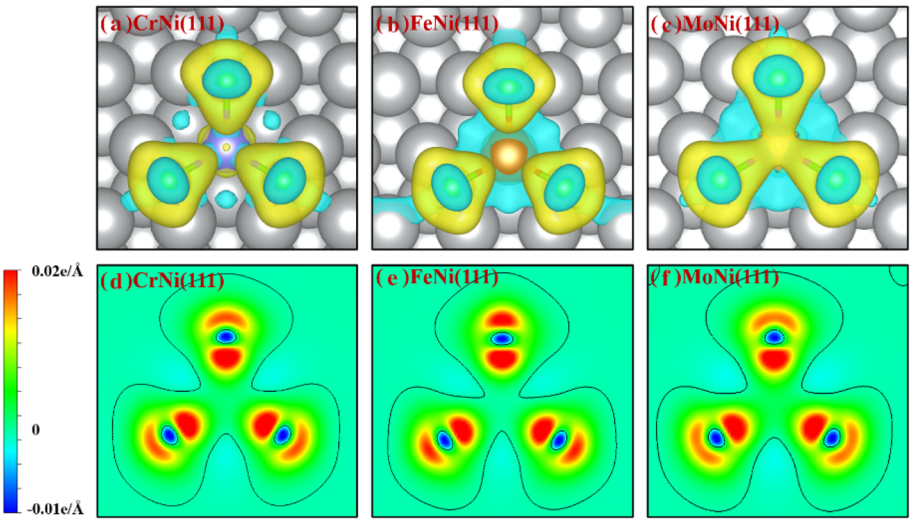

Fig. 6 Differential charge density diagram of (a) Cr, (b) Fe and (c) Mo on Ni (111) surfaces with MCl_3-type adsorption, in which the silver white sphere is an Ni atom; and (d)–(f) horizontal cross sections at Cl atoms.

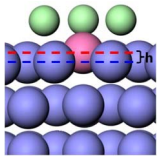

Fig. 7 Cross section of stable adsorption configuration of MCl_3.

indicating that Cr (Fe or Mo) is bonded with Cl atoms, respectively and form MCl_3 corrosion products. The interaction between Ni and Cl around the doped atoms is weak, and no chloride formation of Ni is around the doped atoms.

Fig. 6(d)–(f) show the horizontal cross section at the Cl atom. The darker the red color, the greater the charge density. It can be seen that the red color of Cl near the doped Cr (Fe or Mo) is darker, indicating that the charge density between the Cl and doped Cr (Fe or Mo) is higher, and chemical bonds are formed between Cl and Cr (Fe or Mo).

3.3.3 Desorption of corrosion products. Fig. 7 shows the results of the structural optimization calculation and the formation of corrosion products in MCl_3-type adsorption on M–Ni (111) surface. It is found that the doped atom is significantly higher than the Ni (111) surface (the height is denoted by symbol h). The higher the doped atoms are above the Ni (111) surface, the smaller the desorption energy of the corrosion products, which makes the corrosion products leave the Ni (111) surface easier.

Structural optimization calculations of other types of adsorption such as MCl_2-type and MCl_4-type were also carried out. The calculated h and the desorption energy of MCl_2 and MCl_4 are also listed in Table 8. The formula for the calculation of the desorption energy is as follows:

$$E_{\text{desorption}} = E_{\text{out}} - E_{\text{slab + adsorbate}} \quad (4)$$

where E_{out} is the total energy of MCl_2, MCl_3 or MCl_4 after leaving the surface to the vacuum layer of the simulated system, and $E_{\text{slab + adsorbate}}$ is the total energy of MCl_2, MCl_3 or MCl_4 while they are still on the Ni (111) surface.

Table 8 shows that the h of the Cr atom in $CrCl_4$ is 0.602 Å, which is the highest in the compounds of MCl_2, MCl_3 or MCl_4, indicating that $CrCl_4$ is most likely to leave the Ni (111) crystal plane. The minimum desorption energy of 3.342 eV of $CrCl_4$ among the compounds also supports the above-mentioned inference. The boiling point of $CrCl_4$ is 600 °C,[22] and thus when the Cr-rich alloys were corroded at 600 °C, the $CrCl_4$ formed may leave the metal surface in the form of gas.

The above-mentioned studies show that the doped Cr–Ni (111) crystal surface exhibited a larger adsorption energy for Cl, higher charge transfer amount of absorbed Cl from Cr, and lower desorption energy of corrosion product $CrCl_4$. These results well explain the preferred reaction of Cr and Cl atoms when the M–Ni (111) crystal plane adsorbs Cl atoms. However, it is also necessary to understand the migration ability of doped Cr, Fe or Mo atoms from the inside of the Ni crystal to the surface layer, which is related to the continuous loss of Cr during the corrosion process of the Cr-rich Ni-based alloys.

3.3.4 The effects of adsorption of Cl on the segregation of doped atoms. The segregation difference of doped Cr (Fe or Mo) migrating from the interior of the Ni (111) crystal to the surface layer can characterize the migration ability of these doped atoms. The segregation energy of the doped Cr (Fe or Mo) close to the bulk phase is considered as zero based on the system energy of the doped atom in the fourth layer inward from the Ni surface, as shown in Fig. 1. To simplify the calculation, Cl atoms are adsorbed at the most stable FCC1 site, and the calculation results of segregation energy are shown in Fig. 8.

Fig. 8 shows that in the doped Cr–Ni (111) crystal, compared to unadsorbed Cl, the segregation energy of Cr in the first layer decreases from 0.199 eV to −0.080 eV when Cl is adsorbed on the surface. In crystals doped with Fe–Ni (111) and Mo–Ni (111), the segregation energies of Fe and Mo in the first layer decrease after the surface adsorption of Cl, but their values are all greater than 0.0 eV.

The difference between the segregation energy of the 1st and the 2nd layer doped Cr (Fe or Mo) atom is shown in Table 9.

According to Table 9 and Fig. 8, the results show that the segregation energy difference of Cr from the sub-outer layer to

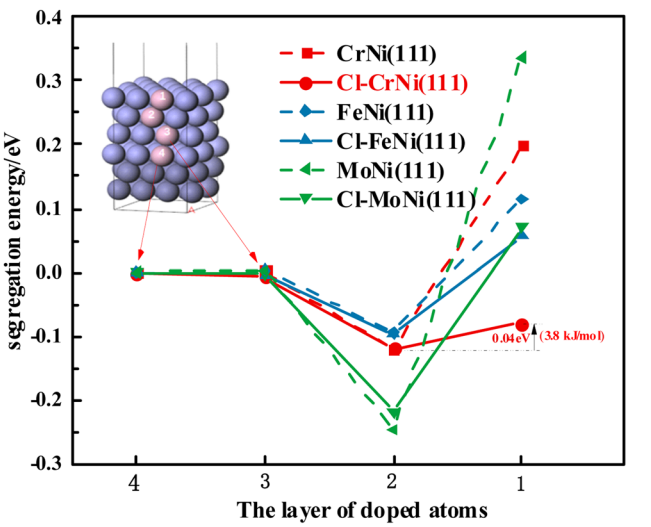

Fig. 8 Segregation energy of different Ni atom stacking layers with Cr, Fe and Mo on Ni (111) surface.

Table 8 Height (h) of doped atoms above the Ni (111) surface and desorption energy

Products	$CrCl_2$	$CrCl_3$	$CrCl_4$	$FeCl_2$	$FeCl_3$	$MoCl_2$	$MoCl_3$	$MoCl_4$
h/Å	0.317	0.479	0.602	0.162	0.242	0.164	0.289	0.401
$E_{\text{desorption}}$/eV	4.023	3.883	3.342	4.455	4.685	6.418	5.147	4.243

Table 9 Segregation energy difference of Cr (Fe or Mo) migrating from the 2nd layer to the 1st layer on Ni (111) surface

Surface	Cr–Ni (111)	Fe–Ni (111)	Mo–Ni (111)	Cl–Cr–Ni (111)	Cl–Fe–Ni (111)	Cl–Mo–Ni (111)
Segregation/eV	0.319	0.208	0.582	0.040	0.152	0.291

the surface layer is only 0.040 eV after the adsorption of Cl compared to 0.319 eV before Cl adsorption, which is 0.040 eV. The Cr atom can overcome this energy difference easily and move to the first layer. This suggests that the Cr atom tends to remain in the bulk phase of Ni when the Cr–Ni (111) surface does not adsorb Cl; after the adsorption of Cl, Cr tends to move to the surface to approach Cl atom, such that the subsequent reaction continues. To some extent, this explains the reason for the preferential loss of Cr when the Cr-rich nickel-based alloy is corroded in the chloride molten salt.

4. Conclusion

In this work, the corrosion behavior of the Cr-rich alloys Hastelloy C-276 and Hastelloy X and Cr-poor alloy Hastelloy B-2 in ternary NaCl–$MgCl_2$–$CaCl_2$ molten salts was studied *via* both experiments and first-principles calculations to systematically illustrate the reaction process of Cl atoms adsorbed on the surface of doped Cr (Fe or Mo)–Ni (111) crystals to explore the mechanism of corrosion. Cr loss was observed in the cross-section of Hastelloy C-276 and Hastelloy X after long-term corrosion in the molten salt, while this phenomenon was not observed in Hastelloy B-2. The $MgCr_2O_4$ protective layer produced by the preferential loss of chromium is the reason why the alloy is more resistant to corrosion.

The first-principles calculations on Cl adsorption show that the Cr–Ni (111) surface exhibits stronger activity than the Fe or Mo doping surface in terms of Cl adsorption, charge transfer, corrosion product desorption, and reduced segregation energy Cl migration from the inner layer of the crystal to the surface layer. These findings indicate that Cl adsorption on the Cr–Ni (111) surface is a key driving force of Cr loss in Cr-rich alloys. This suggests that the corrosion of Cr-rich nickel-based alloys in chloride molten salts can be inhibited if the contact between the chlorine atoms in the molten salts and the metal surface can be reduced. For example, a possible corrosion prevention strategy for alloys in molten salts is *via* the pre-generation of an $MgCr_2O_4$ protective layer. The proposed mechanism of corrosion of Cr-rich nickel alloys in chloride molten salts from several perspectives in this work would provide insights for mitigating the corrosion problem in chloride molten salt applications.

Conflicts of interest

There are no conflicts to declare.

Data availability

Data will be made available upon request.

Supplementary information: the element distribution map images of EDS and adsorption configurations. See DOI: https://doi.org/10.1039/d5ra04910e.

Acknowledgements

The authors would like to acknowledge the financial support provided by the National Natural Science Foundation of China (No. 52036011 and No. U22A20213).

References

1 W. Ding, F. Yang, A. Bonk and T. Bauer, *Sol. Energy Mater. Sol. Cells*, 2021, **223**, 110979–110988.
2 S. S. Raiman and S. Lee, *J. Nucl. Mater.*, 2018, **511**, 523–535.
3 X. Wang, H. Yin, W. Liu, G. Yu, J. He, Z. Tang and L. Yan, *Mater. Corros.*, 2020, **71**, 931–937.
4 K. Vignarooban, P. Pugazhendhi, C. Tucker, D. Gervasio and A. M. Kannan, *Sol. Energy*, 2014, **103**, 62–69.
5 Q. Liu, Z. Wang, W. Liu, H. Yin, Z. Tang and Y. Qian, *Corros. Sci.*, 2021, **180**, 109183–109188.
6 Q. Gong, A. Hanke, F. Kessel, A. Bonk, T. Bauer and W. Ding, *Sol. Energy Mater. Sol. Cells*, 2023, **253**, 112233.
7 B. Liu, X. Wei, W. Wang, J. Lu and J. Ding, *Sol. Energy Mater. Sol. Cells*, 2017, **170**, 77–86.
8 M. Alkhamis, Master's Degree Dissertation, University of Arizona, 2016.
9 J. E. Indacochea, J. L. Smith, K. R. Litko, E. J. Karell and A. G. Raraz, *Oxid. Met.*, 2001, **55**, 1–16.
10 Y. Yu, W. Xiao, J. Wang and L. Wang, *Phys. Chem. Chem. Phys.*, 2016, **18**, 26616–26622.
11 Y.-R. Yin, C.-L. Ren, H. Han, J.-X. Dai, H. Wang, P. Huai and Z.-Y. Zhu, *Phys. Chem. Chem. Phys.*, 2018, **20**, 28832–28839.
12 H. O. Nam, A. Bengtson, K. Vortler, S. Saha, R. Sakidja and D. Morgan, *J. Nucl. Mater.*, 2014, **449**, 148–157.
13 A. D. Clark, W. L. Lee, A. R. Solano, T. B. Williams, G. S. Meyer, G. J. Tait, B. C. Battraw and S. D. Nickerson, *J. Phys. Chem. B*, 2021, **125**, 211–218.
14 R. Chahal, S. Roy, M. Brehm, S. Banerjee, V. Bryantsev and S. T. Lam, *JACS Au*, 2022, **2**, 2693–2702.
15 B. A. Frandsen, S. D. Nickerson, A. D. Clark, A. Solano, R. Baral, J. Williams, J. Neuefeind and M. Memmott, *J. Nucl. Mater.*, 2020, **537**, 152219–152233.
16 D. Sprouster, G. Zheng, S.-C. Lee, D. Olds, C. Agca, J. McFarlane and B. Khaykovich, *ACS Appl. Energy Mater.*, 2022, **5**, 8067–8074.
17 M. Salanne, C. Simon, P. Turq and P. A. Madden, *J. Fluorine Chem.*, 2009, **130**, 38–44.
18 S.-C. Lee, Y. Zhai, Z. Li, N. P. Walter, M. Rose, B. J. Heuser and Y. Zhang, *J. Phys. Chem. B*, 2021, **125**, 10562–10570.
19 C. S. Sona, M. A. Khanwale, C. S. Mathpati, A. Borgohain and N. K. Maheshwari, *Appl. Therm. Eng.*, 2014, **70**, 451–461.
20 J. Startt, R. Dingreville, S. S. Raiman and C. Deo, *Appl. Surf. Sci.*, 2021, **563**, 149836–149847.
21 S. Guo, J. Zhang, W. Wu and W. Zhou, *Prog. Mater. Sci.*, 2018, **97**, 448–487.

22 X. Wei, X. Zhang, J. Ding, W. Wang and J. Lu, *Energy Procedia*, 2019, **158**, 773–778.
23 ASTM G1-03. Standard practice for preparing, cleaning, and evaluating corrosion test specimens, 2011 corrosion test specimens, the ASTM website, **https://www.astm.org**, 2011.
24 G. Kresse and J. Hafner, *Phys. Rev. B:Condens. Matter Mater. Phys.*, 1993, **47**, 558–561.
25 G. Kresse and J. Hafner, *Phys. Rev. B:Condens. Matter Mater. Phys.*, 1994, **49**, 14251–14269.
26 G. Kresse and J. Furthmuller, *Comput. Mater. Sci.*, 1996, **6**, 15–50.
27 J. P. Perdew, K. Burke and M. Ernzerhof, *Phys. Rev. Lett.*, 1997, **78**, 1396.
28 P. E. Blochl, *Phys. Rev. B:Condens. Matter Mater. Phys.*, 1994, **50**, 17953–17979.
29 G. Kresse and D. Joubert, *Phys. Rev. B:Condens. Matter Mater. Phys.*, 1999, **59**, 1758–1775.
30 R. Tran, Z. Xu, B. Radhakrishnan, D. Winston, W. Sun, K. A. Persson and S. P. Ong, *Sci. Data*, 2016, **3**, 160080.
31 H. B. Michaelson, *J. Appl. Phys.*, 1977, **48**, 4729–4733.